



# Solar Energetic Electron Events Associated with Hard X-Ray Flares

Wen Wang<sup>1</sup>, Linghua Wang<sup>1</sup>, Säm Krucker<sup>2,3</sup>, Glenn M. Mason<sup>4</sup>, Yang Su<sup>5,6</sup>, and Radoslav Bučík<sup>7</sup><sup>1</sup> School of Earth and Space Sciences, Peking University, Beijing, 100871, People's Republic of China; [wanglh@pku.edu.cn](mailto:wanglh@pku.edu.cn), [wanglh@pku.edu.cn](mailto:wanglh@pku.edu.cn)<sup>2</sup> Space Sciences Laboratory, University of California at Berkeley, Berkeley, CA 94720, USA<sup>3</sup> Institute of 4D Technologies, University of Applied Sciences Northwestern Switzerland, 5210 Windisch, Switzerland<sup>4</sup> Applied Physics Laboratory, Johns Hopkins University, Laurel, MD 20723, USA<sup>5</sup> Key Laboratory of Dark Matter and Space Astronomy, Purple Mountain Observatory, Chinese Academy of Sciences (CAS), Nanjing, 210023, People's Republic of China<sup>6</sup> School of Astronomy and Space Science, University of Science and Technology of China, Hefei, 230026, People's Republic of China<sup>7</sup> Southwest Research Institute, San Antonio, TX 78238, USA

Received 2020 November 7; revised 2021 March 15; accepted 2021 March 16; published 2021 May 27

## Abstract

We investigate 16 solar energetic electron (SEE) events measured by WIND/3DP with a double-power-law spectrum and the associated western hard X-ray (HXR) flares measured by RHESSI with good count statistics, from 2002 February to 2016 December. In all the 16 cases, the presence of an SEE power-law spectrum extending down to  $\leq 5$  keV at 1 au implies that the SEE source would be high in the corona, at a heliocentric distance of  $\geq 1.3$  solar radii, while the footpoint or footpoint-like emissions shown in HXR images suggest that the observed HXRs are likely produced mainly by HXR-producing electrons via thick-target bremsstrahlung processes very low in the corona. We find that for all the 16 cases, the estimated power-law spectral index of HXR-producing electrons is no less than the observed high-energy spectral index of SEEs, and it shows a positive correlation with the high-energy spectral index of SEEs. In addition, the estimated number of SEEs is only  $\sim 10^{-4}$ – $10^{-2}$  of the estimated number of HXR-producing electrons at energies above 30 keV, but with a positive correlation between the two numbers. These results suggest that in these cases, SEEs are likely formed by upward-traveling electrons from an acceleration source high in the corona, while their downward-traveling counterparts may undergo a secondary acceleration before producing HXRs via thick-target bremsstrahlung processes. In addition, the associated  ${}^3\text{He}/{}^4\text{He}$  ratio is positively correlated with the observed high-energy spectral index of SEEs, indicating a possible relation of the  ${}^3\text{He}$  ion acceleration with high-energy SEEs.

*Unified Astronomy Thesaurus concepts:* Solar energetic particles (1491); Solar flares (1496)

## 1. Introduction

Solar energetic electron (SEE) events have been measured in situ in the interplanetary medium (IPM) since the 1960s (e.g., van Allen & Krimigis 1965; Anderson & Lin 1966), showing a typical double-power-law energy spectrum at energies from hundreds of keV down to  $\sim$ keV with a downward break energy around 60 keV (Lin et al. 1982; Krucker et al. 2009). The estimated occurrence rate of SEE events over the whole Sun reaches  $\sim 10^4$  events  $\text{yr}^{-1}$  at solar maximum (Wang et al. 2012), making the SEE events the most common solar particle acceleration phenomenon observed in the IPM. Wang et al. (2012) reported that  $\sim 76\%$  of SEE events are accompanied with low-energy ( $\sim$ MeV) ion emissions that are highly enriched in  ${}^3\text{He}$  ( ${}^3\text{He}/{}^4\text{He} \geq 0.01$ ). The electron/ ${}^3\text{He}$ -rich events form the class of “impulsive” solar energetic particle (SEP) events, so-called because the associated flare soft X-ray (SXR) bursts, when present, are impulsive (with a duration of  $< 1$  hr) (Cane et al. 1986). Many studies proposed that electron/ ${}^3\text{He}$ -rich SEP events are accelerated in flares (see Reames 1999 for a review).

Lin (1985) reported that  $\sim 45\%$  of impulsive SEE events observed at energies above  $\sim 15$  keV are accompanied by detectable hard X-ray (HXR) bursts. These HXR flare bursts generally have strong emissions originating from footpoints of

flares loops (e.g., Dennis 1988; Krucker et al. 2011), also with a single-power-law or double-power-law energy spectrum (e.g., Lin & Schwartz 1987; Krucker et al. 2007a). According to the statistical studies of HXR flares (Dulk et al. 1992; Alaoui et al. 2019), the double-power-law HXR spectra generally have a downward break energy typically around 100 keV, similar to the downward break energy of double-power-law SEE spectra (Krucker et al. 2009). Therefore, many studies (e.g., Reames 1999; Shimojo & Shibata 2000; Lin 2006) further proposed that in flares, some accelerated electrons travel along the open magnetic field line to form SEEs in the IPM, while the other accelerated electrons propagate downward and collide with ambient dense plasma to generate HXRs via bremsstrahlung mechanisms (e.g., Brown 1971). Lin (1974), Pan et al. (1984), and Krucker et al. (2007a) found that the estimated number of electrons escaping upwards to the IPM is only  $\sim 0.1\%$ – $1\%$  of the estimated number of electrons traveling downwards to generate HXRs. In addition, Krucker et al. (2007a) found a close positive correlation between the power-law spectral index  $\beta$  of impulsive SEEs and index  $\gamma$  of associated HXRs, both observed at energies above 50 keV. But such a correlation did not match with either classical thick-target ( $\gamma = \beta - 1$ ) or thin-target ( $\gamma = \beta + 1$ ) bremsstrahlung predictions.

Moreover, previous timing studies (e.g., Krucker et al. 1999, 2007a; Maia & Pick 2004; Klein et al. 2005) showed that at energies above  $\sim 25$  keV, some SEE events are “prompt” (i.e., the inferred release onset of  $\geq 25$  keV electrons coincides with the release timing of associated HXR flares/type III radio bursts), but most events are “delayed” (i.e., the inferred release

**Table 1**  
Spectral Parameters of SEEs and Associated HXR Flares

#	Date	SEEs						HXR Flares								
		$T_{\text{Rel}}^{\text{b}}$ (Hour)	$\beta_1$	$\beta_2$	$E_B^{\text{c}}$ (keV)	$N_{\text{SEE}} (\times 10^{33})$		$T_{\text{HXR}}^{\text{c}}$ (UT)	Interval <sup>d</sup> (UT)	Class <sup>e</sup>	Location <sup>f</sup> (Deg)	$\gamma$ & $\gamma_1, \gamma_2$	$E_B^{\text{HXR}}$ (keV)	$\beta^{\text{HPE}}$	$N_{\text{HPE}} (\times 10^{35})$	
						>30 keV	>50 keV								>30 keV	>50 keV
(1)	(2)	(3)	(4)	(5)	(6)	(7)	(8)	(9)	(10)	(11)	(12)	(13)	(14)	(15)	(16)	(17)
1	20020220	11.0	$1.95 \pm 0.08$	$3.2 \pm 0.4$	$52 \pm 17$	$1.2_{-3.5}^{+1}$	$0.49_{-1.4}^{+0.39}$	10:57:58	10:56:12- 10:59:04	C7.5	N15W81	$3.1 \pm 0.1,$ $3.9 \pm 0.2$	$46 \pm 4$	$4.1 \pm 0.1$	$25 \pm 9$	$3.5 \pm 1.2$
2	20020411	16.3	$2.16 \pm 0.05$	$4.5 \pm 0.5$	$46 \pm 12$	$12_{-10}^{+34}$	$4.1_{-3.3}^{+3}$	16:11:52	16:07:40- 16:17:24	C9.2	S11W33	$3.6 \pm 0.2$	...	$4.6 \pm 0.2$	$13 \pm 4$	$1.6 \pm 0.5$
3	20020530	5.1	$2.45 \pm 0.05$	$4.3 \pm 0.9$	$65 \pm 23$	$9.5_{-27}^{+7.6}$	$3.0_{-8.7}^{+2.4}$	05:10:48	04:59:20- 05:16:04	M1.3	N9West <sup>g</sup>	$5.2 \pm 0.2$	...	$6.2 \pm 0.2$	$42 \pm 11$	$1.5 \pm 0.4$
4	20020602	10.2	$1.56 \pm 0.05$	$3.7 \pm 0.7$	$48 \pm 13$	$1.7_{-4.8}^{+1.4}$	$0.58_{-1.7}^{+0.47}$	10:05:48	09:56:16- 10:11:40	C8.0	S20W60	$2.9 \pm 0.2,$ $3.6 \pm 0.4$	$39 \pm 9$	$3.7 \pm 0.1$	$19 \pm 11$	$2.7 \pm 1.5$
5 <sup>a</sup>	20020804	15.0	$2.16 \pm 0.14$	$3.7 \pm 0.7$	$59 \pm 21$	$3.6_{-10}^{+2.9}$	$1.2_{-3.4}^{+0.94}$	14:48:42	14:44:32- 14:49:48	C4.8	S15West <sup>g</sup>	$4.8 \pm 0.1$	...	$5.8 \pm 0.1$	$14 \pm 2.3$	$1.3 \pm 0.2$
6	20020927	1.4	$1.61 \pm 0.04$	$3.7 \pm 0.4$	$86 \pm 20$	$23_{-65}^{+18}$	$10_{-30}^{+8.4}$	01:17:42	01:12:52- 01:23:16	C5.0	S17West <sup>g</sup>	$3.9 \pm 0.1$	...	$4.8 \pm 0.1$	$9.9 \pm 4.6$	$1.3 \pm 0.6$
7 <sup>a</sup>	20030318	12.1	$1.93 \pm 0.04$	$3.9 \pm 0.4$	$92 \pm 23$	$88_{-250}^{+70}$	$32_{-90}^{+25}$	11:53:35	11:48:04- 12:14:00	X1.5	S10W47	$5.3 \pm 0.1$	...	$6.2 \pm 0.1$	$1600 \pm 280$	$110 \pm 31$
8	20030930	8.7	$2.07 \pm 0.06$	$4.1 \pm 0.4$	$64 \pm 12$	$0.97_{-2.8}^{+0.77}$	$0.36_{-1}^{+0.29}$	08:40:38	08:40:12- 08:43:28	C3.2	N03W44	$4.3 \pm 0.1$	...	$5.2 \pm 0.1$	$14 \pm 3.3$	$1.1 \pm 0.3$
9	20031002	3.9	$2.76 \pm 0.05$	$5.4 \pm 1.1$	$62 \pm 18$	$0.28_{-0.79}^{+0.22}$	$0.063_{-0.18}^{+0.05}$	03:49:10	03:47:56- 03:50:00	C2.4	N05W71	$5.5 \pm 0.1$	...	$6.4 \pm 0.1$	$2.8 \pm 0.6$	$0.16 \pm 0.03$
10	20040228	3.2	$2.38 \pm 0.05$	$5.4 \pm 0.9$	$94 \pm 22$	$1.5_{-4.4}^{+1.2}$	$0.39_{-1.1}^{+0.31}$	03:15:50	03:15:16- 03:16:36	B6.6	N18W50	$4.2 \pm 0.1$	...	$5.0 \pm 0.1$	$3.1 \pm 0.5$	$0.26 \pm 0.04$
11	20041101	3.3	$1.53 \pm 0.06$	$4.5 \pm 0.5$	$58 \pm 10$	$7.8_{-22}^{+6.3}$	$2.9_{-8.3}^{+2.3}$	03:10:45	03:09:24- 03:15:16	M1.1	N10W47	$3.4 \pm 0.1,$ $4.5 \pm 0.2$	$40 \pm 3$	$4.8 \pm 0.1$	$47 \pm 15$	$5.2 \pm 1.6$
12	20061117	22.2	$2.00 \pm 0.06$	$5.2 \pm 0.9$	$56 \pm 12$	$3.8_{-11}^{+3}$	$1.1_{-3.1}^{+0.86}$	22:23:47	22:20:00- 22:25:24	B2.4	S08W48	$4.0 \pm 0.1$	...	$4.8 \pm 0.1$	$3.6 \pm 1.5$	$0.4 \pm 0.2$
13	20110809	7.9	$1.66 \pm 0.04$	$3.2 \pm 0.4$	$108 \pm 24$	$30_{-86}^{+24}$	$15_{-43}^{+12}$	07:53:47	07:52:32- 07:59:28	X6.9	N14W67	$2.5 \pm 0.2,$ $3.3 \pm 0.1$	$71 \pm 8$	$3.5 \pm 0.1$	$530 \pm 20$	$86 \pm 3$
14 <sup>a</sup>	20111021	13.0	$2.17 \pm 0.09$	$4.0 \pm 0.7$	$49 \pm 17$	$0.65_{-1.9}^{+0.52}$	$0.23_{-0.65}^{+0.18}$	12:47:38	12:46:40- 12:51:56	M1.3	N05W79	$3.8 \pm 0.1,$ $4.3 \pm 0.2$	$29 \pm 4$	$4.9 \pm 0.1$	$32 \pm 19$	$3.5 \pm 2.0$
15	20140418	12.7	$1.89 \pm 0.06$	$3.3 \pm 0.3$	$62 \pm 17$	$22_{-63}^{+18}$	$9.8_{-28}^{+7.9}$	12:45:45	12:42:32- 12:52:24	M7.3	S14W32	$3.1 \pm 0.1$	...	$3.9 \pm 0.1$	$57 \pm 2$	$11 \pm 0.4$
16	20160720	22.0	$1.76 \pm 0.04$	$5.1 \pm 0.5$	$72 \pm 14$	$50_{-140}^{+40}$	$12_{-33}^{+9.4}$	21:58:50	21:56:36- 22:06:28	C4.6	N02W37	$4.0 \pm 0.2$	...	$5.0 \pm 0.3$	$18 \pm 4$	$1.4 \pm 0.4$

**Notes.**<sup>a</sup> Delayed cases.<sup>b</sup> The solar release time of SEEs is estimated from the onset in the event's highest energy channel detected in situ at 1 au.<sup>c</sup> The peak time of HXRs is obtained after subtracting a 500 s photon travel time along 1 au.<sup>d</sup> The time interval used to calculate  $N_{\text{HPE}}$ , after subtracting a 500 s photon travel time along 1 au.<sup>e</sup> Data from the GOES flare list (<ftp://ftp.swpc.noaa.gov/pub/warehouse/>).<sup>f</sup> Data from the RHESSI flare list (<https://hesperia.gsfc.nasa.gov/rhessi3/data-access/rhessi-data/flare-list/index.html>).<sup>g</sup> Limb-flare cases.

onset of  $\gtrsim 25$  keV electrons is delayed by  $\gtrsim 10$  minutes). In addition, Wang et al. (2006b, 2016) found that in SEE events, the inferred release of  $\gtrsim 15$  keV electrons often start with an average delay of  $\sim 20$  minutes after that of  $\lesssim 10$  keV electrons. Some studies proposed that these observed delays of high-energy SEEs could be related to a secondary acceleration of electrons to high energies (e.g., Wang et al. 2006b; Krucker et al. 2007a) and/or the electron escaping process after acceleration (e.g., Masson et al. 2013, 2019).

On the other hand, recent studies reported that many electron/ $^3\text{He}$ -rich SEP events are associated with fast narrow coronal mass ejections (CMEs)/jets (Wang et al. 2006a; Pick et al. 2006; Wang et al. 2012, 2016; Bučik 2020). Wang et al. (2016), Mason et al. (2016), and Mason & Klecker (2018) proposed that  $^3\text{He}$  could be accelerated by some processes related to narrow CMEs or jets that likely originate from interchange reconnection (e.g., Shimojo & Shibata 2000; Bučik et al. 2018). Timing studies also showed that the estimated solar release of  $^3\text{He}$ -rich ions appears to be delayed after the release of SEEs by  $\sim 1$  hour (Ho et al. 2003; Wang et al. 2016), when the associated CME reaches an average altitude of  $\sim 4.7R_s$  (Wang et al. 2016). Therefore, the generation of electrons, HXR, and  $^3\text{He}$ -rich ions in these SEP events is more complex than previously thought.

In this paper, we examine the particle energy spectra in 16 good SEE event with the associated HXR flares, observed by the Wind 3D Plasma and Energetic Particle (3DP) instrument and the Reuven Ramaty High Energy Solar Spectroscopic Imager (RHESSEI), in order to build up an improved generation scenario of SEEs/HXRs (and possible  $^3\text{He}$ -rich ions) in these SEP events.

## 2. Observations

The WIND spacecraft was launched on 1994 November 1. Since then, the 3D Plasma and Energetic Particle (3DP) instrument (Lin et al. 1995) on WIND has provided high-resolution measurements of electron three-dimensional distributions with an energy range from solar wind thermal plasma to  $\sim 400$  keV. The Silicon Semiconductor Telescopes (SSTs) measure  $\sim 25$ – $400$  keV electrons with an energy channel resolution of  $\Delta E/E = 0.3$  and pitch angle resolution of  $22^\circ.5$ . The electron electrostatic analyzers (EESA-L and EESA-H) measure  $\sim 3$  eV– $30$  keV electrons with an energy channel resolution of  $\Delta E/E = 0.2$  and pitch angle resolution of  $22^\circ.5$ . In this paper, we also utilize the solar X-ray observations at energies of 3 keV to 300 keV from RHESSEI (Lin et al. 2002), and the  $^3\text{He}/^4\text{He}$  ratio measurements at energies of  $\sim 0.5$ – $2$  MeV nucleon $^{-1}$  from the Ultra Low Energy Isotope Spectrometer (ULEIS) on the Advanced Composition Explorer (ACE) spacecraft (Mason et al. 1998).

### 2.1. Event Selection

After surveying the in situ electron measurements by WIND/3DP at 1 au in the IPM and the remote measurements of solar X-rays by RHESSEI from 2002 February through 2016 December, we found 507 SEE events observed at energies above 15 keV with the RHESSEI data available around the solar release time of the SEE event,  $T_{\text{Rel}}$ , that is estimated by subtracting the travel time along the nominal Parker spiral field length from the in situ onset observed in the event highest energy channel (Wang et al. 2012). Since the inferred solar

injection of high-energy electrons often start with an average delay of  $\sim 20$  minutes after that of low-energy electrons in SEE events (Wang et al. 2006b, 2016), we define an HXR flare burst to be associated with an SEE event, if  $|T_{\text{HXR}} - T_{\text{Rel}}| < 20$  min, where  $T_{\text{HXR}}$  is the maximum time of HXR burst estimated by subtracting a 500 s photon travel time from the in situ maximum time observed in the flare’s highest energy channel. Among these 507 SEE events, 237 (47%) have an associated HXR flare, consistent with previous studies (Lin 1985).

In order to make a comprehensive comparison of the spectral parameters (e.g., low-energy and high-energy spectral indexes, break energy) between the SEEs and associated HXR, we use the following criteria to select good SEE-HXR cases: (1) a clear velocity dispersion of SEEs indicating a nearly scatter-free propagation along the nominal Parker spiral field line, (2) a good double-power-law spectrum of SEE peak flux versus energy at energies from  $\leq 5$  keV to  $\sim 200$  keV, (3) a good HXR peak (characterized with the presence of clear rise and decay) spectrum at energies from  $\leq 25$  keV to  $\geq 40$  keV with a flare location at solar longitude  $W30^\circ$ – $W90^\circ$  that magnetically connects to the vicinity of the Earth (Wang et al. 2012). Among the 237 SEE events with associated HXR flares, 190, 52, and 57 events satisfy, respectively, Criteria #1, #2, and #3, while the 16 events satisfying all three criteria are selected for this comprehensive study (Table 1). As suggested by Krucker et al. (2007a), the selected 16 cases can be further classified into two groups: 13 prompt cases with  $T_{\text{Rel}} - T_{\text{HXR}} \leq 10$  minutes and 3 delayed cases with  $T_{\text{Rel}} - T_{\text{HXR}} > 10$  minutes.

Figure 1 shows one representative prompt SEE-HXR case observed on 2004 November 1. This SEE event observed by Wind/3DP exhibits a clear velocity dispersion at all energies from 2.8 keV to 310 keV (panel (a)), and a double-power-law spectrum of peak flux versus energy that bends down at a break around 58 keV (panel (b)). The velocity dispersion analysis of electron peak times at energies above 25 keV gives an electron path length estimate of  $L = 1.4 \pm 0.2$  au (panel (c)), consistent with the nominal Parker spiral field length from the Sun to spacecraft. The associated HXR flare is located at  $N10^\circ W47^\circ$  (panel (f)) and shows a double-power-law spectrum of peak flux versus energy at energies from  $\sim 20$  keV to  $\sim 100$  keV that bends down at a break around 40 keV. Figure 2 shows one representative delayed SEE-HXR case observed on 2002 August 4. This case also exhibits a clear velocity dispersion of SEEs at energies from 6.1 keV to 180 keV (panel (a)), a double-power-law spectrum of SEE peak flux versus energy that bends down at a break around 59 keV (panel (b)), and an associated HXR flare located on the western limb (panel (d)).

### 2.2. SEEs

#### 2.2.1. Energy Spectrum

For the selected 16 cases (see Figure 1 for an example), the peak flux of SEEs fits well to a double-power-law energy spectrum described as follows:

$$J_e \propto \begin{cases} E^{-\beta_1}, & E < E_B^e \\ E^{-\beta_2}, & E > E_B^e \end{cases} \quad (1)$$

where  $J_e$  is the electron peak differential flux after subtracting the pre-event background,  $E_B^e$  is the spectral break energy, and  $\beta_1$  ( $\beta_2$ ) is the power-law index at energies below (above)  $E_B^e$ . After considering the uncertainties both in electron flux and

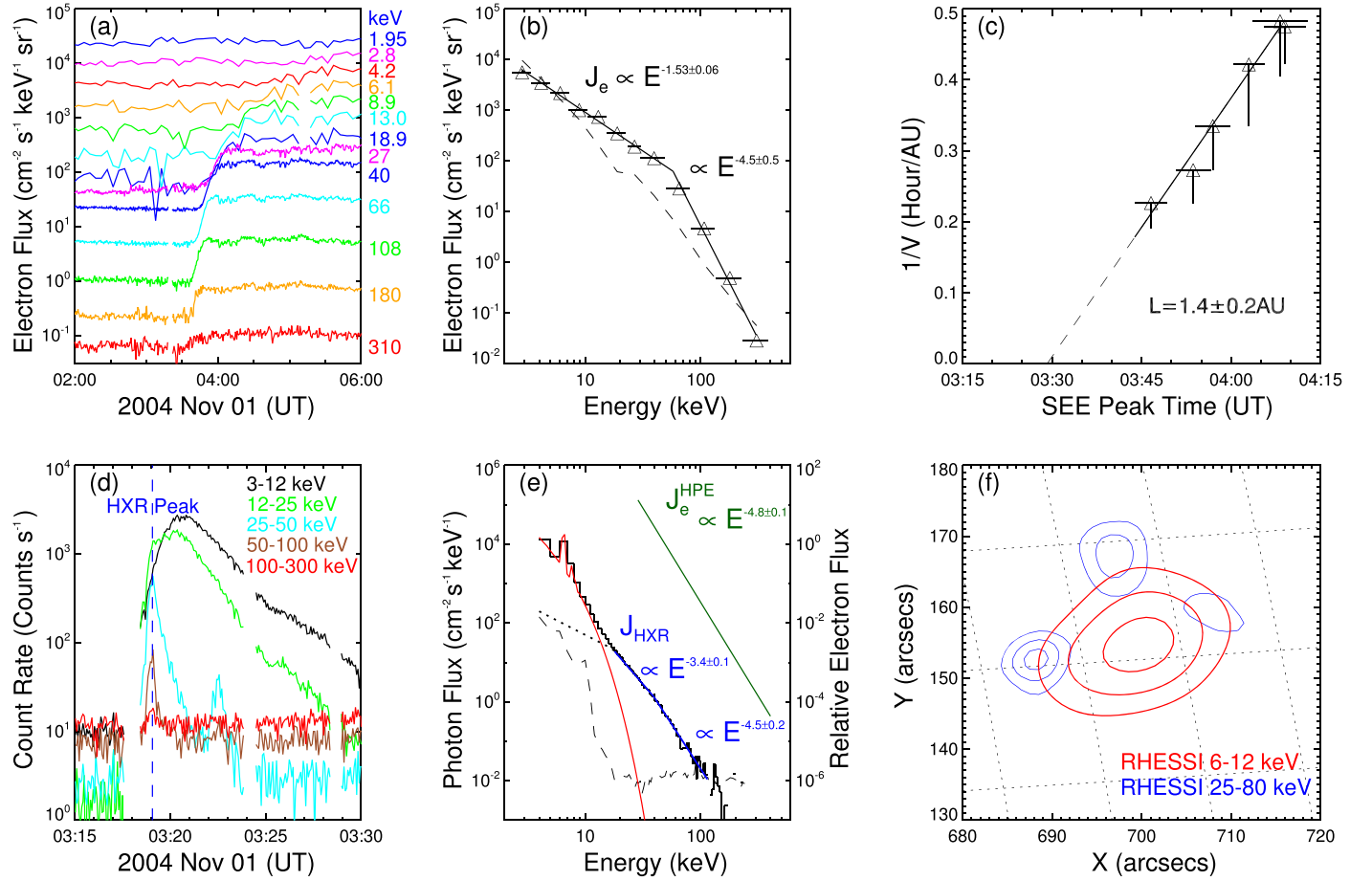


**Figure 1.** Overview of the 2004 November 1 SEE-HXR case. Panel (a): fluxes of outward-traveling electrons observed at 1.95–18.9 keV (5 minute average) by EESA-H and at 27–310 keV by SST (30 s average). Panel (b): the SEE spectrum of peak flux vs. energy (triangles), after subtracting the pre-event fluxes (black dashed curve). The straight line indicates the double-power-law fit to the peak flux spectrum. Panel (c): the velocity dispersion analysis of electron peak times (triangles) at energies above 25 keV, using the lower bound of the energy channel to calculate the velocity of electrons in the peak. Panel (d): X-ray count rates of the associated HXR flare observed by RHESSI. The vertical blue dashed line denoting the HXR peak time. Panel (e): the HXR spectrum of peak flux vs. energy (black solid curve) observed by RHESSI Detector 4, after subtracting the pre-event fluxes (black dashed curve). The red curve shows the thermal fit with a  $T_e \sim 24$  MK and  $EM \sim 2.9 \times 10^{47} \text{ cm}^{-3}$ , dominated in observations at energies below  $\sim 15$  keV. The blue line represents a double-power-law fit to observations at energies above 17 keV. The black dotted line shows a power-law spectrum with a fixed index of 1.5, as an approximation of nonthermal emissions below 17 keV (e.g., Krucker et al. 2007a, 2007b; Krucker & Lin 2008). The green straight line indicates a single-power-law spectrum of HPEs (multiplied by an arbitrary factor for clarity of display) estimated from the HXR peak spectrum under relativistic thick-target bremsstrahlung model. Panel (f): RHESSI CLEAN image (Hurford et al. 2002) with X-ray intensity contours at levels of 50%, 70%, and 90%.

energy (Liu et al. 2020), the  $E_B^e$  ranges from  $\sim 50$  keV to  $\sim 110$  keV,  $\beta_1$  ranges from 1.5 to 2.8, and  $\beta_2$  ranges from 3.2 to 5.4 (see Table 1), with a positive correlation between  $\beta_1$  and  $\beta_2$  (Figure 4(f)). These results are similar to the statistical study of SEE spectra by Krucker et al. (2009). The positive correlation between  $\beta_1$  and  $\beta_2$  may carry important information on the acceleration processes of SEEs at low energies and at high energies.

For each SEE event, we calculate the total number of electrons in the IPM,  $N_{\text{SEE}}$ , by integrating the background-subtracted electron flux over the event duration, energy and antisunward solid angle, and by assuming a spatial cone of  $45^\circ$  wide, according to a statistical study of SEEs over 11 years (Wang et al. 2012). The uncertainties of  $N_{\text{SEE}}$  can be estimated by varying the conic angular extent from  $20^\circ$  to  $90^\circ$ . For all the 16 cases (Table 1),  $N_{\text{SEE}}$  is  $\sim 10^{32}$ – $10^{35}$  ( $\sim 10^{31}$ – $10^{34}$ ) at energies above 30 keV (50 keV).

The 13 prompt cases behave almost the same as all the selected 16 cases together (Figures 4 and 5; Table 1). For the three delayed cases (shown as solid symbols in Figures 4 and 5),

the break energy  $E_B^e$  ranges from  $\sim 50$  keV to  $\sim 90$  keV, low-energy spectral index  $\beta_1$  ranges from 1.9 to 2.2, high-energy spectral index  $\beta_2$  ranges from 3.7 to 4.0, and electron number  $N_{\text{SEE}}$  is  $\sim 10^{33}$ – $10^{35}$  ( $\sim 10^{32}$ – $10^{34}$ ) at energies above 30 keV (50 keV), similar to the 13 prompt cases. However, the three delayed cases show no correlation between  $\beta_1$  and  $\beta_2$ , different from the prompt cases.

### 2.2.2. Source Region of SEEs

During the propagation from the Sun to the spacecraft in the IPM, electrons will lose energy due to Coulomb collisions and the ambipolar electrostatic potential between the Sun and IPM (Wang et al. 2006b):

$$\begin{aligned} \frac{dE}{dr} &= \left( \frac{dE}{dr} \right)_{\text{COL}} + \left( \frac{dE}{dr} \right)_{\text{AEP}} \\ &= -1.82 \times 10^{-7} \frac{n(r)}{E} - \frac{0.994}{r^2}, \end{aligned} \quad (2)$$

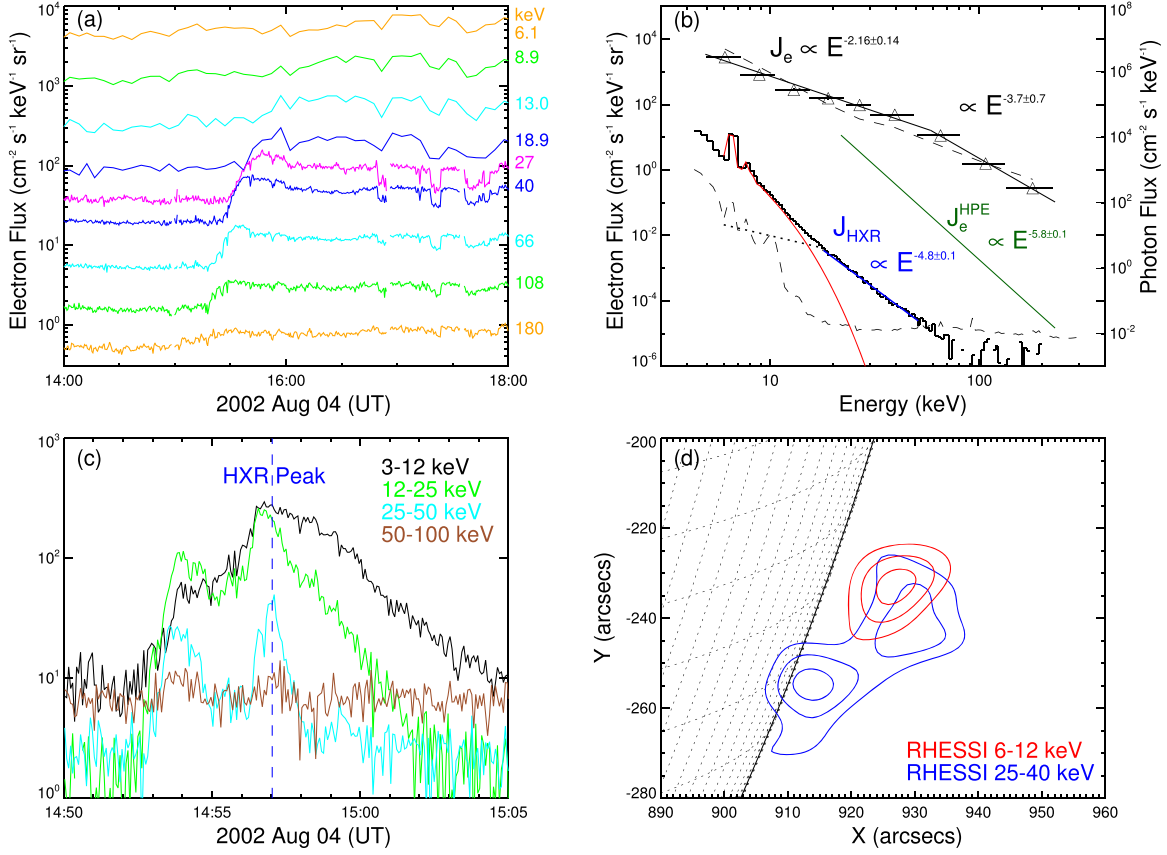


**Figure 2.** Overview of the 2002 August 4 SEE-HXR case. Panel (a): fluxes of outward-traveling electrons observed at 6.1–18.9 keV (5 minute average) by EESA-H and at 27–180 keV by SST (30 s average). Panel (b): the peak flux energy spectra of SEEs (triangles) and HXR (black solid curve), with the pre-event fluxes (black dashed lines) subtracted. HXR is observed by RHESSI Detector 4. The black straight line indicates the double-power-law fit to the SEE spectrum. The red curve shows the thermal fit with a  $T_e \sim 20$  MK and  $EM \sim 3.3 \times 10^{47} \text{ cm}^{-3}$  to the X-ray spectrum at energies below  $\sim 15$  keV, while the blue line represents a single-power-law fit to the HXR spectrum at energies above  $\sim 17$  keV. The black dotted line is a power-law shape with a fixed index of 1.5 as an approximation of nonthermal emissions below 17 keV (e.g., Krucker et al. 2007a, 2007b; Krucker & Lin 2008). The green straight line indicates a single-power-law spectrum of HPEs (multiplied by an arbitrary factor for clarity of display) estimated from the HXR peak spectrum under the relativistic thick-target bremsstrahlung model. Panel (c): X-ray count rates of the associated HXR flare observed by RHESSI. The vertical blue dashed line denotes the HXR peak time. Panel (d): RHESSI CLEAN image with X-ray intensity contours at levels of 50%, 70%, and 90%.

where  $r$  is the heliocentric distance in solar radius  $R_s$ , and  $n(r)$  is the plasma number density in  $\text{cm}^{-3}$  from the corona to solar wind as defined by Leblanc et al. (1998) and Mann et al. (1999):

$$n(r) = \begin{cases} 2.0 \times 10^9 e^{13.83(\frac{1}{r}-1)}, & \text{if } 1.02 \leq r < 3; \\ 3.3 \times 10^5 r^{-2} + 4.1 \times 10^6 r^{-4} + 8.0 \times 10^7 r^{-6}, & \text{if } 3 \leq r < 215. \end{cases} \quad (3)$$

Assuming an electron energy spectrum at the source altitude  $r_0$ , we can derive the electron spectrum in the IPM after considering the above energy loss processes during the propagation. Figure 3 shows that if the source spectrum at the Sun has a double-power-law form, the predicted low-energy spectrum at 1 au would bend down below a higher energy for a lower source altitude, while the predicted high-energy spectrum at 1 au remains unchanged.

All the selected 16 cases (including both prompt and delayed cases) exhibit a low-energy power-law spectrum extending down to  $\leq 5$  keV (see Figure 1(b) for an example). Simulations show that to retain such a low-energy spectrum observed at 1 au would require a solar source at the heliocentric distance of  $\geq 1.3 R_s$  (Figure 3). This suggests that these SEEs (especially at

low energies) likely originate from a source high in the corona, consistent with the previous studies (e.g., Potter et al. 1980; Wang et al. 2012, 2016).

### 2.3. HXR<sub>s</sub>

#### 2.3.1. Energy Spectrum of HXR<sub>s</sub>

The peak flux of HXR<sub>s</sub> at energies above  $\sim 10$ – $15$  keV can fit to a double-power-law function:

$$J_{\text{HXR}} \propto \begin{cases} E^{-\gamma_1}, & E < E_B^{\text{HXR}} \\ E^{-\gamma_2}, & E > E_B^{\text{HXR}}, \end{cases} \quad (4)$$

or to a single-power-law function:

$$J_{\text{HXR}} \propto E^{-\gamma}, \quad (5)$$

where  $J_{\text{HXR}}$  is HXR peak flux after subtracting the pre-event background,  $\gamma$  is the power-law index for the single-power-law

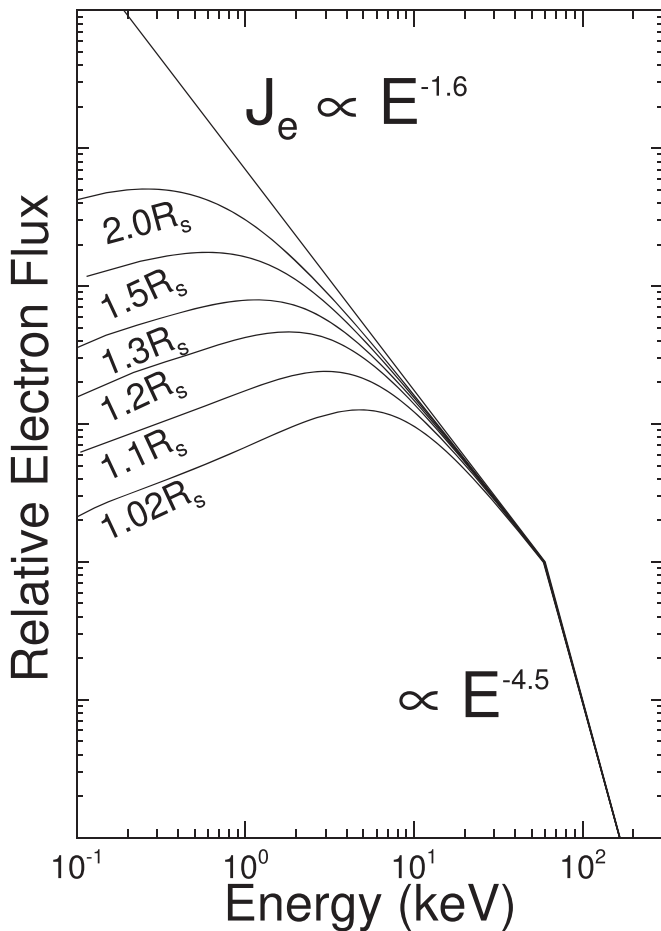


**Figure 3.** Simulated electron spectra at 1 au derived from a double-power-law spectrum injected at different heliocentric altitudes in the solar corona. The shown spectral indexes are the estimated spectral indexes of electrons at an altitude of  $\sim 1.3 R_s$  for the 2004 November 1 SEE event, after considering the electron energy loss due to Coulomb collisions and the ambipolar electrostatic potential between the Sun and IPM.

spectrum, and  $\gamma_1$  ( $\gamma_2$ ) is the power-law index at energies below (above) the break energy  $E_B^{\text{HXR}}$  for the double-power-law spectrum. Note that all these observed HXR spectra have been corrected for the pile-up and albedo effects (e.g., Smith et al. 2002; Kontar et al. 2006).

Among the 16 cases, 5 HXR flares with HXR measurements at energies up to  $\sim 100$ – $200$  keV exhibit a double-power-law energy spectrum that has an  $E_B^{\text{HXR}}$  ranging from  $\sim 30$  keV to  $\sim 70$  keV, a  $\gamma_1$  ranging from 2.5 to 3.8 and  $\gamma_2$  ranging from 3.3 to 4.5, while the other 11 HXR flares with HXR measurements at energies up to  $\sim 80$  keV show a single-power-law spectrum that has a  $\gamma$  ranging from 3.1 to 5.5 (Table 1). For example, the (prompt) 2004 November 1 case shows a double-power-law HXR spectrum at  $\sim 15$ – $115$  keV that is fitted with a  $\gamma_1$  of  $3.4 \pm 0.1$  at energies below  $E_B^{\text{HXR}} = 40 \pm 3$  keV and a  $\gamma_2$  of  $4.5 \pm 0.2$  at energies above (Figure 1(e)), while the (delayed) 2002 August 4 case has a single-power-law HXR spectrum at  $\sim 15$ – $50$  keV that is fitted with a  $\gamma$  of  $4.8 \pm 0.1$  (Figure 2(b)). The observed HXR spectral parameters are consistent with previous statistical studies (e.g., Dulk et al. 1992; Alaoui et al. 2019).

The 13 prompt cases behave almost the same as all the 16 cases together (Figure 4; Table 1). Among the three delayed cases, one case shows a double-power-law HXR spectrum with a  $\gamma_1$  of  $3.8 \pm 0.1$  at energies below an  $E_B^{\text{HXR}}$  of  $29 \pm 4$  keV and a  $\gamma_2$  of  $4.3 \pm 0.2$  at energies above, while two cases show a single-power-law HXR spectrum with a  $\gamma$  of 4.8–5.3 (see Figure 2(b) for an example). These results are similar to those of the 13 prompt cases.

### 2.3.2. HXR-producing Electrons

Among the selected 16 cases, 13 HXR flares are clearly located on the western solar disk (Figure 1(f)) and three HXR flares appear to be located on or beyond the western limb (Figure 2(d)), all showing a footpoint or footpoint-like source/sources. For the 2004 November 1 flare located at  $N10^\circ W47^\circ$  (Figure 1(f)), the RHESSI X-ray imaging exhibits three HXR footpoint sources (blue contours) plus a thermal looptop source (red contours) at the HXR peak time, consistent with the interchange-reconnection flare scenario (e.g., Shimojo & Shibata 2000). For the 2002 August 4 flare on the western limb (Figure 2(d)), the X-ray imaging shows two HXR sources (blue contours) including a weaker HXR looptop source that overlaps with a thermal looptop source (red contours) and a stronger HXR footpoint-like source. For all the selected cases, therefore, HXR observations are likely dominated by emissions generated via thick-target bremsstrahlung processes at low altitudes.

For each case, we use the RHESSI relativistic thick-target bremsstrahlung model to derive the energy spectrum of HXR-producing electrons (HPEs) from the observed HXR energy spectrum. Instead of a double-power-law spectrum, we assume that the HPE differential flux,  $J_e^{\text{HPE}}$ , is a single-power-law function of energy described as

$$J_e^{\text{HPE}} \propto E^{-\beta^{\text{HPE}}}, \quad (6)$$

where  $\beta^{\text{HPE}}$  is the power-law spectral index, since using a double-power-law function does not give a significantly different estimate of spectral indexes for the selected cases. For the 16 cases, the fitted  $\beta^{\text{HPE}}$  varies from 3.5 to 6.4 (Table 1 and Figure 4), e.g.,  $4.8 \pm 0.1$  for the 2004 November 1 case and  $5.8 \pm 0.1$  for the 2002 August 4 case.

For each case, we also use the relativistic thick-target bremsstrahlung model to estimate the total number,  $N_{\text{HPE}}$ , of suprathermal electrons that are needed to produce the observed HXR emissions (e.g., Krucker et al. 2007a; James et al. 2017). The estimated  $N_{\text{HPE}}$  is  $\sim 10^{35}$ – $10^{38}$  at energies above 30 keV and  $\sim 10^{34}$ – $10^{37}$  at energies above 50 keV (Table 1 and Figure 5).

In this study, we use the highest energy of SEEs measured by Wind/3DP at 1 au, instead of a default value of 32 MeV (Holman 2003), as a realistic estimate of the high-energy cutoff of electrons,  $E_{\text{max}}^{\text{HPE}}$ , to derive HPEs under the RHESSI bremsstrahlung models. When  $E_{\text{max}}^{\text{HPE}}$  is changed to 32 MeV (not shown), the estimated spectral index  $\beta^{\text{HPE}}$  remains similar in 14 cases and increases by  $\sim 10\%$  in the other two cases, while the estimated electron number  $N_{\text{HPE}}$  remains similar in all the 16 cases.

Moreover, the 13 prompt cases behave almost the same as all the 16 cases together (Figures 4 and 5; Table 1). For the three delayed cases,  $\beta^{\text{HPE}}$  ranges from 4.9 to 6.2, while  $N_{\text{HPE}}$  is

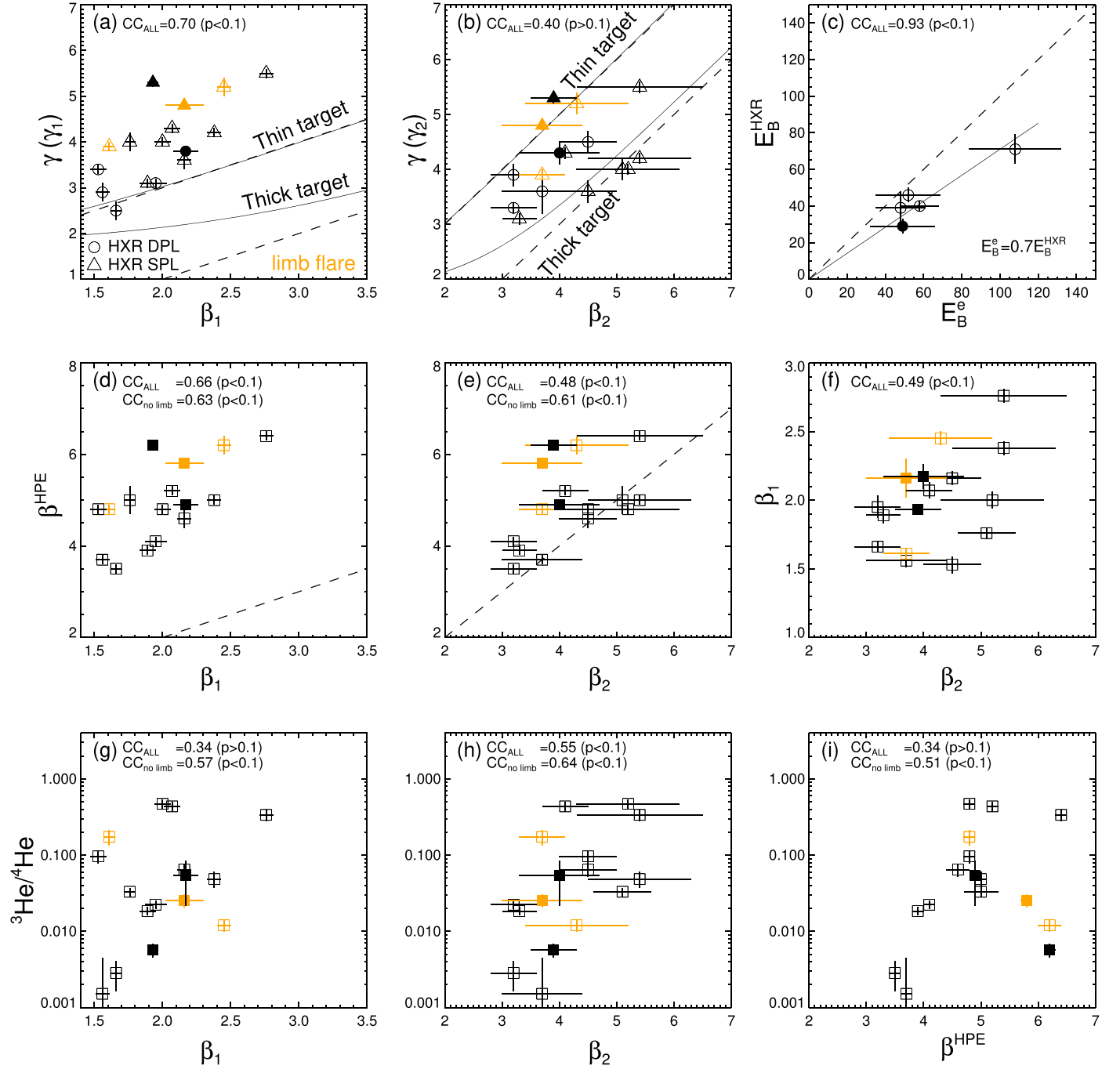


**Figure 4.** Scatter diagrams of the selected 16 SEE-HXR cases. Panel (a): the low-energy HXR spectral index,  $\gamma$  or  $\gamma_1$ , vs. low-energy SEE spectral index  $\beta_1$ . Panel (b): the high-energy HXR spectral index,  $\gamma$  or  $\gamma_2$ , vs. high-energy SEE spectral index  $\beta_2$ . In panels (a)–(b), the black solid (dashed) line represents classical (relativistic) thin-target/thick-target bremsstrahlung spectral relations between electrons and HXRs. Panel (c): the fitted HXR spectral break energy vs. SEE spectral break energy. In panels (a)–(c), triangles show the 11 cases with a single-power-law (SPL) HXR spectrum, while circles represent the other five cases with a double-power-law (DPL) HXR spectrum. Panel (d): the estimated HPE spectral index  $\beta^{HPE}$  vs.  $\beta_1$ . Panel (e):  $\beta^{HPE}$  vs.  $\beta_2$ . In panels (c)–(e), the dashed line indicates the 1:1 ratio. Panel (f):  $\beta_1$  vs.  $\beta_2$ . Panels (g)–(i): the associated  ${}^3\text{He}/{}^4\text{He}$  ratio vs.  $\beta_1$ ,  $\beta_2$  and  $\beta^{HPE}$ . In panels (d)–(i), all 16 cases are indicated by squares. In all these panels, orange symbols mark the three limb-flare cases; open symbols show the prompt cases, while solid symbols denote the delayed cases.

$\sim 10^{36}$ – $10^{38}$  at energies above 30 keV and  $\sim 10^{35}$ – $10^{37}$  at energies above 50 keV, similar to the 13 prompt cases.

#### 2.4. Comparison between SEEs and HXRs

Among the selected 16 cases with a double-power-law energy spectrum of SEEs, five exhibit a double-power-law energy spectrum of HXRs. For these five cases (Figures 4(a)–(c) and Table 2), the HXR spectral break energy  $E_B^{HXR}$  and SEE

break energy  $E_B^e$  appear to be positively correlated (correlation coefficient<sup>8</sup>  $CC = 0.93$ ), with a linear regression line of  $E_B^{HXR} = (0.7 \pm 0.1)E_B^e$ . At energies below the break

<sup>8</sup> Only statistically significant CCs are listed in the manuscript text. A CC is statistically significant when its probability  $p$  (p-value) is less than 0.1 (Reames et al. 1988). For a statistically significant CC, it indicates no relationship when  $|CC| < 0.3$ ; it indicates a weak, moderate, and strong relationship, respectively, when  $0.3 \leq |CC| < 0.5$ ,  $0.5 \leq |CC| < 0.7$ , and  $|CC| \geq 0.7$ .

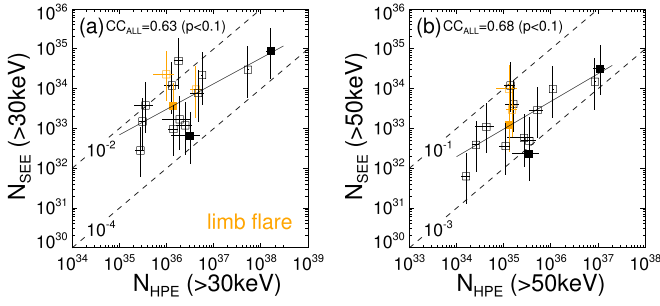


**Figure 5.** Scatter diagrams of the total number of escaping electrons in the IPM and the total number of HPEs in HXR flares at energies beyond 30 keV (panel (a)) and 50 keV (panel (b)). Open symbols show the prompt cases, while solid symbols denote the delayed cases. The dashed lines denote the ratios of  $10^{-4}$ ,  $10^{-3}$ ,  $10^{-2}$ , or  $10^{-1}$ . Orange symbols show the three limb-flare cases. The solid lines represent a linear regression of  $N_{\text{HPE}} = (2.3 \pm 2.8) \times 10^{10} \times N_{\text{SEE}}^{0.64 \pm 0.29}$  in panel (a) and of  $N_{\text{HPE}} = (4.6 \pm 38) \times 10^8 \times N_{\text{SEE}}^{0.69 \pm 0.27}$  in panel (b).

**Table 2**

CCs<sup>a</sup> between SEEs and HXRs for HXR DPL Events and SPL Events

	SEE		
	$\beta_1$	$\beta_2$	$E_B^e$
	$\gamma_1$		
HXR DPL	$\gamma_2$	CC = 0.82	
	$E_B^{\text{HXR}}$		CC = 0.93
HXR SPL	$\gamma$	CC = 0.59	

<sup>a</sup> Only statistically significant CCs (with  $p < 0.1$ ) are listed in the table.

(Figure 4(a)), the HXR spectral index  $\gamma_1$  shows no clear correlation with the SEE spectral index  $\beta_1$ . Compared with the bremsstrahlung predictions based on  $\beta_1$ ,  $\gamma_1$  agrees with classic (dashed line) and relativistic (solid line) thin-target predictions in one case and is significantly larger than thin-target predictions in the other four cases, while  $\gamma_1$  is much larger than classic and relativistic thick-target predictions in all five cases. At energies above the break (Figure 4(b)), the HXR index  $\gamma_2$  has a positive correlation (CC = 0.82) with the SEE index  $\beta_2$ , with a linear regression equation of  $\gamma_2 = (0.98 \pm 0.53)\beta_2 + (0.32 \pm 1.98)$ . Compared with the bremsstrahlung predictions based on  $\beta_2$ ,  $\gamma_2$  agrees with classic and relativistic thin-target predictions in one case and with the relativistic thick-target prediction in another case, while  $\gamma_2$  lies between thin-target and thick-target predictions in the other three cases.

The other 11 cases show a single-power-law energy spectrum of HXRs. For these 11 cases (Figures 4(a)–(b) and Table 2), the HXR spectral index  $\gamma$  appears to be positively correlated (CC = 0.59) with the SEE spectral index  $\beta_1$ , with a linear regression equation of  $\gamma = (2.06 \pm 0.17)\beta_1 + (0.08 \pm 0.37)$ , but  $\gamma$  is significantly larger than both thin-target and thick-target predictions according to  $\beta_1$  (Figure 4(a)). For the SEE spectral index  $\beta_2$ ,  $\gamma$  shows no clear correlation;  $\gamma$  agrees with classic/relativistic thin-target predictions in three cases and with classic/relativistic thick-target predictions in four cases, while  $\gamma$  appears to lie between thin-target and thick-target predictions in the other four cases (Figure 4(b)).

Assuming a single-power-law spectral shape, the estimated spectral index of HPEs via the relativistic thick-target model,  $\beta^{\text{HPE}}$ , shows a positive correlation with both the observed SEE spectral index  $\beta_1$  at energies below  $E_B^e$  and index  $\beta_2$  at energies

above (Figures 4(d)–(e) and Table 3). For all the 16 cases,  $\beta^{\text{HPE}}$  is much larger than  $\beta_1$ , while the presence of a positive correlation between  $\beta_1$  and  $\beta^{\text{HPE}}$  can come from the positive correlation between  $\beta_1$  and  $\beta_2$  (see Section 2.2.1). It likely indicates no relationship between HPEs and low-energy SEEs. Among the 16 cases,  $\beta^{\text{HPE}}$  is similar to  $\beta_2$  in eight cases and significantly larger than  $\beta_2$  in the other eight cases. These results suggest a close relationship between HPEs and high-energy SEEs in the selected cases. Note that all three limb flares (orange symbols) have a  $\beta^{\text{HPE}}$  significantly larger than  $\beta_2$ , suggesting that the HXR generation in these flares may not be described well by thick-target model.

At energies above 30 keV (Figure 5(a)), the estimated number of SEEs,  $N_{\text{SEE}}$ , is positively correlated with the estimated number of HPEs via the relativistic thick-target model,  $N_{\text{HPE}}$ , with a linear regression line of  $N_{\text{HPE}} \propto N_{\text{SEE}}^{0.6 \pm 0.3}$ , while  $N_{\text{SEE}}$  is only  $\sim 10^{-4}$ – $10^{-2}$  ( $\sim 6 \times 10^{-3}$  on average) of  $N_{\text{HPE}}$ . At energies above 50 keV (Figure 5(b)),  $N_{\text{SEE}}$  is also positively correlated with  $N_{\text{HPE}}$  with a linear regression line of  $N_{\text{HPE}} \propto N_{\text{SEE}}^{0.7 \pm 0.3}$ , while  $N_{\text{SEE}}$  is only  $\sim 10^{-3}$ – $10^{-1}$  ( $\sim 2 \times 10^{-2}$  on average) of  $N_{\text{HPE}}$ .

The 13 prompt cases show almost the same results as all the 16 cases together (Figures 4 and 5; Tables 1 and 3). Compared to the 13 prompt cases, the 3 delayed cases appear to behave similarly in the relationship of the electron number and spectral break energy between SEEs and HXRs/HPEs. At energies above 30 keV (50 keV), however, the average  $N_{\text{SEE}}/N_{\text{HPE}}$  ratio for the three delayed cases is  $\sim 10^{-3}$  ( $\sim 4 \times 10^{-3}$ ), about 7 times (5 times) smaller than the average  $N_{\text{SEE}}/N_{\text{HPE}}$  ratio of  $\sim 7 \times 10^{-3}$  ( $\sim 2 \times 10^{-2}$ ) for the 13 prompt cases. For the three delayed cases, the spectral indexes of HXRs/HPEs show no clear correlation with the SEE spectral indexes, different from the prompt cases, while the high-energy HXR spectral index agrees with classic and relativistic thin-target predictions.

### 2.5. Association with Other Phenomena

As suggested by Wang et al. (2012), we calculate the average  ${}^3\text{He}/{}^4\text{He}$  ratio observed by ACE/ULEIS at  $\sim 0.5$ – $2$  MeV nucleon $^{-1}$  as the associated  ${}^3\text{He}/{}^4\text{He}$  ratio for an SEE event, in a time window that starts 5 hr after the estimated solar electron release and ends 9 hr later or 5 hr after the release of the next SEE event (which ever occurs sooner; see Table 4). Among the selected 16 cases, 13 are accompanied by large  ${}^3\text{He}$  enhancements with the  ${}^3\text{He}/{}^4\text{He}$  ratio  $> 0.01$ , while the other three cases are associated with  ${}^3\text{He}/{}^4\text{He} < 0.01$  (that may still reflect enhanced  ${}^3\text{He}$  emissions, considering that the detection threshold varies with the event intensity and background level (Mason et al. 1999)). For the 16 cases (Figure 4 and Table 3), the associated  ${}^3\text{He}/{}^4\text{He}$  ratio shows a positive correlation (CC = 0.55) with the observed high-energy spectral index of SEEs,  $\beta_2$ , but has no clear correlation with the low-energy spectral index of SEEs,  $\beta_1$ . After excluding three limb-flare cases (that are not in agreement with thick-target prediction), the associated  ${}^3\text{He}/{}^4\text{He}$  ratio also shows a positive correlation (CC = 0.51, Figure 4(f)) with the estimated spectral index of HPEs,  $\beta^{\text{HPE}}$ , probably due to the positive correlation between  $\beta_2$  and  $\beta^{\text{HPE}}$ .

As suggested by Wang et al. (2012), we define a CME to be associated with an SEE event, if the CME is below  $\sim 10 R_S$  at the estimated SEE release at the Sun. Out of the 15 cases with the SOHO/LASCO coverage (Table 4), 12 have a west-limb CME, two have a halo CME, and one has no CME. Among the

**Table 3**  
CCs<sup>a</sup> among SEEs, HXR, and <sup>3</sup>He/<sup>4</sup>He for Prompt Events, Delayed Events, and All Events

		SEE			Ions	
		$\beta_1$	$\beta_2$	$\log(N_{SEE}) (\geq 30\text{keV})$	$\log(N_{SEE}) (\geq 50\text{keV})$	$\log(^3\text{He}/^4\text{He})$
	$\gamma$ and $\gamma_1$	CC <sub>ALL</sub> = 0.70 CC <sub>prompt</sub> = 0.80	CC <sub>ALL</sub> = 0.49 CC <sub>prompt</sub> = 0.68			CC <sub>prompt</sub> = 0.56
	$\gamma$ and $\gamma_2$	CC <sub>ALL</sub> = 0.59 CC <sub>prompt</sub> = 0.66	CC <sub>prompt</sub> = 0.58	CC <sub>prompt</sub> = -0.51	CC <sub>prompt</sub> = -0.57	
HXR	$\log(N_{HPE})$ $\geq (30 \text{ keV})$	CC <sub>prompt</sub> = -0.51	CC <sub>ALL</sub> = -0.60 CC <sub>prompt</sub> = -0.72	CC <sub>ALL</sub> = 0.63 CC <sub>prompt</sub> = 0.57	CC <sub>ALL</sub> = 0.67 CC <sub>prompt</sub> = 0.64	CC <sub>ALL</sub> = -0.66 CC <sub>prompt</sub> = -0.66
	$\log(N_{HPE})$ $\geq (50 \text{ keV})$	CC <sub>ALL</sub> = -0.54 CC <sub>prompt</sub> = -0.64	CC <sub>ALL</sub> = -0.69 CC <sub>prompt</sub> = -0.79	CC <sub>ALL</sub> = 0.62 CC <sub>prompt</sub> = 0.58	CC <sub>ALL</sub> = 0.68 CC <sub>prompt</sub> = 0.66	CC <sub>ALL</sub> = -0.66 CC <sub>prompt</sub> = -0.65
	$\beta^{HPE}$	CC <sub>ALL</sub> = 0.66 CC <sub>prompt</sub> = 0.75	CC <sub>ALL</sub> = 0.48 CC <sub>prompt</sub> = 0.68			CC <sub>prompt</sub> = 0.57
Ions	$\log(^3\text{He}/^4\text{He})$		CC <sub>ALL</sub> = 0.55 CC <sub>prompt</sub> = 0.55	CC <sub>delayed</sub> = -0.99	CC <sub>delayed</sub> = -0.99	

**Note.**

<sup>a</sup> Only statistically significant CCs (with  $p < 0.1$ ) are listed in the table.

12 west-limb CME cases, eight have a CME angular width  $< 90^\circ$ . The two halo-CME cases are accompanied by a reported GOES  $> 10$  MeV proton event. In addition, all 16 cases have a solar/interplanetary radio burst, but only four have an interplanetary type II burst observed by Wind/WAVES.

The 13 prompt cases behave almost the same as all the 16 cases together (Figure 4; Tables 3 and 4). The delayed three cases show no clear correlation between the <sup>3</sup>He/<sup>4</sup>He ratio and the electron spectral index, different from the 13 prompt cases. Among the delayed three cases, all have a west-limb CME, two have a type II radio burst, and none have a GOES  $> 10$  MeV proton event, similar to the prompt cases.

### 3. Summary and Discussion

Among the 507 SEEs observed by WIND/3DP from 2002 through 2016 that have the RHESSI data available, 237 (47%) have an associated HXR flare. We investigate 16 SEE-HXR cases with a double-power-law spectrum of SEEs at energies from  $\leq 5$  keV to  $\sim 200$  keV and a western HXR flare at energies from  $\leq 25$  keV to  $\geq 40$  keV. Among the 16 cases, the power-law spectral index of HPEs estimated via the relativistic thick-target bremsstrahlung model with a finite maximum energy,  $\beta^{HPE}$ , appears to be positively correlated with the observed high-energy spectral index of SEEs above the break,  $\beta_2$ ;  $\beta^{HPE}$  is similar to  $\beta_2$  in eight cases but is significantly larger than  $\beta_2$  in the other eight cases. At energies above 30 keV (50 keV), the estimated number of SEEs,  $N_{SEE}$ , is positively correlated with the estimated number of HPEs,  $N_{HPE}$ , but  $N_{SEE}$  is only  $\sim 10^{-4}$ – $10^{-2}$  ( $\sim 10^{-3}$ – $10^{-1}$ ) of  $N_{HPE}$ . On the other hand, the lower-energy power-law spectrum of SEEs extends down to  $\leq 5$  keV, indicating the presence of a high-corona source of SEEs at  $\geq 1.3 R_S$ , in the 16 cases. These results suggest that in these cases, SEEs are likely formed by upward-traveling electrons from an acceleration source high in the corona, while their downward-traveling counterparts may undergo a secondary acceleration to produce HXR via thick-target bremsstrahlung processes.

Among the 16 cases, 5 HXR flares exhibit a double-power-law energy spectrum and the other 11 HXR flares show a single-power-law spectrum (Table 1). For the five cases with a double-power-law HXR spectrum (Figure 4 and Table 2), the fitted HXR break energy  $E_B^{HXR}$  is positively correlated with the SEE break energy  $E_B^e$ , with a linear regression line of  $E_B^{HXR} = (0.7 \pm 0.1)E_B^e$ . For all 16 cases (Figures 4 and 5; Table 3), high-energy SEEs also show a positive relationship with HPEs, in terms of spectral index and integrated electron number density. However,  $N_{SEE}$  is only orders of magnitude smaller than  $N_{HPE}$ . These results suggest that in the selected 16 cases, SEEs and HPEs are unlikely of the same accelerated population as previously thought, but they are closely related.

In all the selected 16 cases, the source height of SEEs is estimated to be a heliocentric distance of  $\geq 1.3 R_S$  (Figure 3), using a plasma number density model with a given value of  $\sim 6 \times 10^8 \text{ cm}^{-3}$  at  $1.1 R_S$ . Considering a density range of  $\sim 10^8$ – $6 \times 10^8 \text{ cm}^{-3}$  at  $1.1 R_S$  observed for active regions (Aschwanden & Action 2001), the estimated source height of SEEs is  $\sim 1.1$ – $1.3 R_S$ . However, the RHESSI HXR images of 16 HXR flares all show footpoint or footpoint-like emissions, suggesting that the observed HXR are likely produced mainly by thick-target bremsstrahlung processes very low in the corona. If these SEEs and HPEs are, respectively, the upward-traveling and downward-traveling parts of the same accelerated population, merely transportation effects between the HXR-producing region low in the corona and the SEE source region high in the corona cannot retain an electron power-law spectrum at low energies (Figure 3). Therefore, the electron propagation between these regions can involve a secondary acceleration process.

There are two possible generation scenarios for the selected SEE-HXR cases. In one scenario (Figure 6(a)), the electron acceleration first occurs low in the corona, e.g., in flares. Some of the accelerated electrons travel downwards and collide with the dense solar atmosphere to generate HXR, while their upward-traveling counterparts undergo a secondary acceleration high in the corona before escaping to form the SEEs in the IPM. However, this scenario can hardly explain a very small

**Table 4**  
SEEs Associated with Other Solar Phenomena

#	Date	Ions			IP Radio Bursts <sup>b</sup>		Solar Radio Bursts <sup>c</sup>		CME <sup>d</sup>		
		<sup>3</sup> He/ <sup>4</sup> He <sup>e</sup>	ULEIS Period <sup>f</sup> (Hour)	GOES Proton Event <sup>g</sup>	Type III	Type II	Type III	Type II	P. A.	Width	Velocity
(1)	(2)	(3)	(4)	(5)	(6)	(7)	(8)	(9)	(10)	(11)	(12)
1	20020220	0.022 ± 0.003	16.0–25.0	No	Yes	No	Yes	Yes	317	29	623
2	20020411	0.065 ± 0.013	21.3–6.3	No	Yes	No	Yes	Yes	257	70	540
3	20020530	0.012 ± 0.002	10.1–19.1	No	Yes	No	Yes	No	271	144	1625
4	20020602	0.002 ± 0.003	15.2–24.2	No	Yes	No	Yes	Yes	No Data	No Data	No Data
5 <sup>a</sup>	20020804	0.025 ± 0.005	20.0–25.9	No	Yes	No	Yes	No	241	71	663
6	20020927	0.173 ± 0.039	6.4–14.0	No	Yes	No	No	No	231	59	1502
7 <sup>a</sup>	20030318	0.006 ± 0.001	17.1–26.1	No	Yes	Yes	Yes	Yes	263	209	1601
8	20030930	0.435 ± 0.065	13.7–22.7	No	Yes	No	Yes	No	No Event	No Event	No Event
9	20031002	0.337 ± 0.059	8.9–12.5	No	Yes	No	Yes	No	272	48	181
10	20040228	0.048 ± 0.011	8.2–15.6	No	Yes	No	Yes	No	309	85	397
11	20041101	0.096 ± 0.018	8.3–10.8	No	Yes	No	Yes	Yes	242	192	459
12	20061117	0.469 ± 0.064	27.2–36.2	No	Yes	No	Yes	No	226	64	154
13	20110809	0.003 ± 0.001	12.9–21.9	Yes	Yes	Yes	n/a	n/a	Halo	360	1610
14 <sup>a</sup>	20111021	0.054 ± 0.032	18.0–27.0	No	Yes	Yes	n/a	n/a	252	109	317
15	20140418	0.018 ± 0.002	17.7–26.7	Yes	Yes	Yes	n/a	n/a	Halo	360	1203
16	20160720	0.033 ± 0.004	27.0–36.0	No	Yes	No	n/a	n/a	251	52	426

**Notes.**<sup>a</sup> Delayed cases.<sup>b</sup> From the WIND/WAVES observations at 20 kHz–14 MHz.<sup>c</sup> From the event list of Earth ground radio bursts (<https://www.ngdc.noaa.gov/stp/space-weather/solar-data/solar-features/solar-radio/radio-bursts/tables/spectral-sgd/>) that covers a frequency range of 18 MHz–5 GHz and is available until 2011 January.<sup>d</sup> Data from the SOHO LASCO CME catalog ([http://cdaw.gsfc.nasa.gov/CME\\_list/](http://cdaw.gsfc.nasa.gov/CME_list/)).<sup>e</sup> At 0.5–2 MeV nucleon<sup>-1</sup>.<sup>f</sup> The selected ULEIS time windows for the calculation of <sup>3</sup>He/<sup>4</sup>He ratio. The time starts from the zero hour of the date shown in Column (2)<sup>g</sup> The GOES >10 MeV proton events have the peak flux above 1/(cm<sup>2</sup> s sr) after subtracting the pre-event background. The GOES proton information is available from <ftp://ftp.swpc.noaa.gov/pub/warehouse/>.

ratio of  $N_{SEE}$  over  $N_{HPE}$  in the selected cases. In the other scenario (Figure 6(b)), the electron acceleration first occurs high in the corona, e.g., at  $\geq 1.3 R_S$ . Some of the accelerated electrons travel upwards and escape to form the SEEs in the IPM, and their downward-traveling counterparts (especially at high energies) undergo a secondary acceleration before colliding with the dense solar atmosphere to emit HXR at footpoints. Presumably this latter scenario can account for a very small ratio of  $N_{SEE}$  over  $N_{HPE}$ . Moreover, the estimated spectral shape of HPEs appears to be similar to or steeper than the observed spectral shape of high-energy SEEs. This implies that the secondary acceleration process might be more efficient at lower energies than at higher energies.

For the secondary acceleration process proposed in the second scenario (Figure 6(b)), it could be acceleration in flares, betatron acceleration, and/or electric potential acceleration during the electron downward propagation. We use a simple model of betatron acceleration or electric potential acceleration, as well as propagation effects, to estimate the downward-traveling electron energy spectrum at the HXR-producing region, starting from a double-power-law electron spectrum with a break energy of 60 keV at the SEE source region. Here we set the heliocentric altitude of the SEE source region to be  $1.3 R_S$ , and the heliocentric altitude of the HXR-producing region to be  $1.02 R_S$ , which is the lowest heliocentric distance applicable for the density model (Equation (3)). Note that such an altitude of the HXR-producing region is similar to a typical

loop size (Effenberger et al. 2017), although it is probably higher than the general location of the HXR footpoint emitting region (e.g., Sato 2006).

For the betatron acceleration model, we assume that the local magnetic field  $B$  varies with heliocentric altitude  $r$  as  $B(r) \propto (1 + 9.28(r - 1))^{-3}$ , according to the study of Aschwanden et al. (1999). The estimated electron spectrum at  $1.02 R_S$  retains the high-energy spectral index but has a much larger break energy of  $\sim 600$  keV, compared to the source spectrum at  $1.3 R_S$  (Figure 7(a)). For the potential acceleration model, we assume that a magnetic field-aligned potential drop  $\Delta U$  with a constant electric field is 10 kV between  $1.3 R_S$  and  $1.02 R_S$ , based on the studies of Kan et al. (1983) and Kan & Lyu (1990). The estimated electron spectrum at  $1.02 R_S$  shows a slightly larger break energy of  $\sim 70$  keV and a slightly deeper high-energy spectral index. The simulated change in the high-energy spectral index is similar to the observed change between  $\beta_2$  and  $\beta^{HPE}$  in our cases. On the other hand, the electron escaping processes, e.g., the evolving magnetic field configurations due to reconnections between the CME flux-rope magnetic field lines and ambient open field lines (Masson et al. 2013, 2019), could also change the properties of escaping SEEs. Further investigations will require a very careful modeling including more complex acceleration processes, as well as escaping processes.

In the 16 cases (Figure 4 and Table 3), the associated <sup>3</sup>He/<sup>4</sup>He ratio shows a positive correlation with the observed

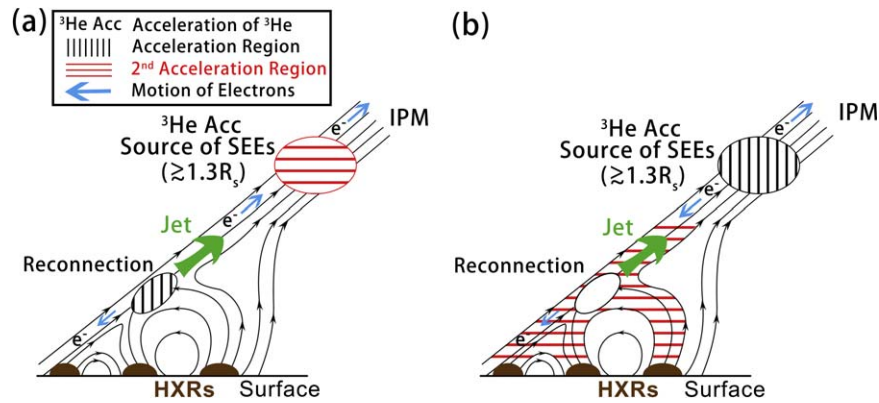


**Figure 6.** Schematics of the two generation scenarios of SEE-HXR cases. Arrowed curves represent the magnetic field lines. Areas shaded with vertical black lines (horizontal red lines) represent the first (secondary) acceleration region. Blue arrows denote the motion of energetic electrons. Green arrows indicate the motion of plasma jets originating from the interchange reconnection.

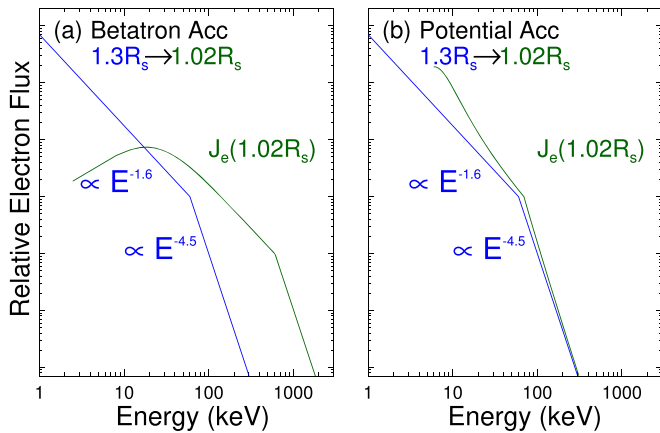


**Figure 7.** The estimated electron spectrum at  $1.02 R_s$  (green curve) after a betatron acceleration and electric potential acceleration between  $1.3 R_s$  and  $1.02 R_s$ . The blue lines show the source electron spectrum with a double-power-law shape at  $1.3 R_s$ .

high-energy spectral index of SEEs,  $\beta_2$ , but has no clear correlation with the low-energy spectral index  $\beta_1$ . This suggests that the acceleration of  $^3\text{He}$  ions may be related to high-energy SEEs, probably occurring high in the corona: the steeper the high-energy electron spectrum, the more efficient the  $^3\text{He}$  ion acceleration. In addition, the majority of these cases are accompanied by a west-limb CME, consistent with previous studies of SEEs (Pick et al. 2006; Wang et al. 2006a, 2012, 2016). As suggested by Wang et al. (2016), Mason et al. (2016), and Mason & Klecker (2018), the associated  $^3\text{He}$ -rich ions could be accelerated by some processes related with CMEs, high in the corona.

As defined by Krucker et al. (2007a), the selected 16 SEE-HXR cases can be classified into two groups: 13 prompt cases with no delayed injection of high-energy SEEs after the release of HXR, and three delayed cases with a clear delayed injection of high-energy SEEs. Unsurprisingly, the 13 prompt cases behave almost the same as all the 16 cases together (Figures 4 and 5; Tables 1 and 3). We find that compared to the 13 prompt cases, the three delayed cases behave differently in the relationship between the spectral indexes: the observed high-energy SEE index  $\beta_2$  shows no clear correlation with the low-energy SEE index  $\beta_1$ ;  $\beta_2$  shows no clear correlation with the observed high-energy HXR spectral index  $\gamma$  or  $\gamma_2$ , while  $\gamma$  or  $\gamma_2$  agrees with thin-target bremsstrahlung predictions; thus,  $\beta_2$

shows no clear correlation with the estimated HPE spectral index  $\beta^{\text{HPE}}$ . Previous studies proposed that in delayed cases, the delayed injection of high-energy SEEs could be due to further acceleration or escaping processes (e.g., Wang et al. 2006b; Krucker et al. 2007a; Masson et al. 2013, 2019). Such acceleration and/or escaping processes may strongly modulate the formation of high-energy SEEs, and thus obscure the relationship of the spectral index between low-energy and high-energy SEEs and between SEEs and HXR/HPEs. For the three delayed cases, therefore,  $\beta_2$  and  $\beta^{\text{HPE}}$  also show no clear correlation with the associated  $^3\text{He}/^4\text{He}$  ratio, and the  $N_{\text{SEE}}/N_{\text{HPE}}$  ratio appears smaller by a factor of  $\sim 5$ , compared to the 13 prompt cases.

This research at Peking University is supported in part by NSFC under contracts 41774183 and 41861134033, and in part by ISSI-BJ and ISSI through the international teams 469 and 425. G.M. is supported in part by NNX17AC05G/125225. Y.S. is supported in part by NSFC under contracts 11820101002 and U1631242. R.B. is supported in part by ACE grant 80NSSC20K1255.

## ORCID iDs

Wen Wang <https://orcid.org/0000-0003-4262-7269>  
 Linghua Wang <https://orcid.org/0000-0001-7309-4325>  
 Säm Krucker <https://orcid.org/0000-0002-2002-9180>  
 Glenn M. Mason <https://orcid.org/0000-0003-2169-9618>  
 Yang Su <https://orcid.org/0000-0002-4241-9921>  
 Radoslav Bućik <https://orcid.org/0000-0001-7381-6949>

## References

- Alaoui, M., Krucker, S., & Saint-Hilaire, P. 2019, *SoPh*, 294, 105  
 Anderson, K. A., & Lin, R. P. 1966, *PhRvL*, 16, 1121  
 Aschwanden, M. J., & Action, L. W. 2001, *ApJ*, 550, 475  
 Aschwanden, M. J., Newmark, J. S., Delaboudinière, J.-P., et al. 1999, *ApJ*, 515, 842  
 Brown, J. C. 1971, *SoPh*, 18, 489  
 Bućik, R. 2020, *SSRv*, 216, 24  
 Bućik, R., Innes, D. E., Mason, G. M., et al. 2018, *ApJ*, 852, 76  
 Cane, H. V., McGuire, R. E., & von Roseninge, T. T. 1986, *ApJ*, 301, 448  
 Dennis, B. R. 1988, *SoPh*, 118, 49  
 Dulk, G. A., Kiplinger, A. L., & Winglee, R. M. 1992, *ApJ*, 389, 756  
 Effenberger, F., Rubio da Costa, F., Oka, M., et al. 2017, *ApJ*, 835, 124  
 Ho, G. C., Roelof, E. C., Mason, G. M., Lario, D., & Mazur, J. E. 2003, *AdSpR*, 32, 2679  
 Holman, G. D. 2003, *ApJ*, 586, 606

- Hurford, G. J., Schmahl, E. J., Schwartz, R. A., et al. 2002, *SoPh*, **210**, 61
- James, T., Subramanian, P., & Kontar, E. P. 2017, *MNRAS*, **471**, 89
- Kan, J. R., Akasofu, S.-I., & Lee, L. C. 1983, *SoPh*, **84**, 153
- Kan, J. R., & Lyu, L. H. 1990, *JGR*, **95**, 4239
- Klein, K. L., Krucker, S., Trotter, G., & Hoang, S. 2005, *A&A*, **431**, 1047
- Kontar, E. P., MacKinnon, A. L., Schwartz, R. A., & Brown, J. C. 2006, *A&A*, **446**, 1157
- Krucker, S., Hannah, I. G., & Lin, R. P. 2007b, *ApJL*, **671**, L193
- Krucker, S., Kontar, E. P., Christe, S., Glesener, L., & Lin, R. P. 2011, *ApJ*, **742**, 82
- Krucker, S., Kontar, E. P., Christe, S., & Lin, R. P. 2007a, *ApJL*, **663**, L109
- Krucker, S., Larson, D. E., & Lin, R. P. 1999, *ApJ*, **519**, 864
- Krucker, S., & Lin, R. P. 2008, *ApJ*, **673**, 1181
- Krucker, S., Oakley, P. H., & Lin, R. P. 2009, *ApJ*, **691**, 806
- Leblanc, Y., Dulk, G. A., & Bougeret, J. 1998, *SoPh*, **183**, 165
- Lin, R. P. 1974, *SSRv*, **16**, 189
- Lin, R. P. 1985, *SoPh*, **100**, 537
- Lin, R. P. 2006, *SSRv*, **124**, 233
- Lin, R. P., Anderson, K. A., Ashford, S., et al. 1995, *SSRv*, **71**, 125
- Lin, R. P., Dennis, B. R., Hurford, G. J., et al. 2002, *SoPh*, **210**, 3
- Lin, R. P., Mewaldt, R. A., & van Hollebeke, M. A. I. 1982, *ApJ*, **253**, 949
- Lin, R. P., & Schwartz, R. A. 1987, *ApJ*, **312**, 462
- Liu, Z. X., Wang, L. H., Wimmer-Schweingruber, R. F., Krucker, S., & Mason, G. M. 2020, *JGRA*, **125**, e28702
- Maia, D. J. F., & Pick, M. 2004, *ApJ*, **609**, 1082
- Mann, G., Jansen, F., MacDowall, R. J., Kaiser, M. L., & Stone, R. G. 1999, *A&A*, **348**, 614
- Mason, G. M., Gold, R. E., Krimigis, S. M., et al. 1998, *SSRv*, **86**, 409
- Mason, G. M., & Klecker, B. 2018, *ApJ*, **862**, 7
- Mason, G. M., Mazur, J. E., & Dwyer, J. R. 1999, *ApJL*, **525**, L133
- Mason, G. M., Nitta, N. V., Wiedenbeck, M. E., & Innes, D. E. 2016, *ApJ*, **823**, 138
- Masson, S., Antiochos, S. K., & Devore, C. R. 2013, *ApJ*, **771**, 82
- Masson, S., Antiochos, S. K., & Devore, C. R. 2019, *ApJ*, **884**, 143
- Pan, L. D., Lin, R. P., & Kane, S. R. 1984, *SoPh*, **91**, 345
- Pick, M., Mason, G. M., Wang, Y.-M., Tan, C., & Wang, L. 2006, *ApJ*, **648**, 1247
- Potter, D. W., Lin, R. P., & Anderson, A. A. 1980, *ApJL*, **236**, L97
- Reames, D. V. 1999, *SSRv*, **90**, 413
- Reames, D. V., Dennis, B. R., & Stone, R. G. 1988, *ApJ*, **327**, 998
- Sato, J. 2006, *AdSpR*, **38**, 968
- Shimojo, M., & Shibata, K. 2000, *ApJ*, **542**, 1100
- Smith, D., Lin, R., Turin, P., et al. 2002, *SoPh*, **210**, 33
- van Allen, J. A., & Krimigis, S. M. 1965, *JGR*, **70**, 5737
- Wang, L., Krucker, S., Mason, G. M., Lin, R. P., & Gang, L. 2016, *A&A*, **585**, A119
- Wang, L., Lin, R. P., Krucker, S., & Gosling, J. T. 2006b, *GeoRL*, **33**, L03106
- Wang, L., Lin, R. P., Krucker, S., & Mason, G. M. 2012, *ApJ*, **759**, 69
- Wang, Y.-M., Pick, M., & Mason, G. M. 2006a, *ApJ*, **639**, 495